Tunnelling and Underground Space Technology 135 (2023) 105033

Contents lists available at ScienceDirect

Tunnelling and Underground Space Technology

journal homepage: www.elsevier.com/locate/tust

Trenchless Technology Research

Identification of deformed configurations of segmental tunnel rings based on measured convergences

Jiao-Long Zhang [a,b], Zijie Jiang [b,a], Xian Liu [a], Yong Yuan [a], Herbert A. Mang [b,a], Bernhard L.A. Pichler [b,*]

[a] College of Civil Engineering, Tongji University, Siping Road 1239, 200092 Shanghai, China
[b] Institute for Mechanics of Materials and Structures, TU Wien, Karlsplatz 13/202, 1040 Vienna, Austria

ARTICLE INFO

Keywords:
Mechanized tunneling
Segmental tunnel linings
Tubbing rings
Kinematic analysis
Real-scale test
Serviceability limit state (SLS)

ABSTRACT

If convergences grow so large that the serviceability of a tubbing ring is lost, remedial measures must be taken. In this context, it is useful to reconstruct the displacement history of the tunnel ring in order to gain insight into the evolution of the structural behavior that has led to the current configuration. This challenge is tackled with the help of measured convergences and rigid body kinematics. The latter are sufficient, because the deformations of tubbings, resulting from normal forces and bending moments, do not contribute significantly to the displacements of segmental rings. The analysis is focused on convergences measured during a real-scale test of a symmetric tunnel ring. It consists of six tubbings and has three kinematic degrees of freedom. Deformed configurations are reproduced by optimizing the *three* scalar components of one symmetric and two antisymmetric modes of rigid body displacements. This problem is under-determined, because convergences are routinely measured in *two* directions only. Its solution is obtained in two steps. At first, the component of the symmetric mode of rigid body displacements is identified such that the measured convergences are reproduced in the best-possible fashion. Thereafter, the remaining differences between measured and modeled convergences are reduced to zero by optimizing the components of the two antisymmetric modes. This kind of structural analysis starts with the most recent set of measured convergences. It proceeds, in a step-by-step manner backwards in time to older sets of monitored data. It is shown that the developed method allows for a satisfactory reproduction of the displacement history of the tested tubbing ring, making use of measured vertical and horizontal convergences. The obtained visualization of the displacement history of the entire tunnel ring provides more insight into the structural behavior than diagrams showing only the evolution of single convergences.

1. Introduction

Tunnel boring machines excavate the ground mass and construct linings consisting of segmental rings. The precast reinforced concrete segments are referred to as tubbings. Right after installation, every ring is supposed to be close to a perfect circle. External forces acting on the lining result in its ovalization (Huang et al., 2017; Marwan et al., 2021). This is routinely monitored by measuring changes of the diameter, i.e. convergences, both in vertical and horizontal direction (Pinto and Whittle, 2014). Ovalization of segmental linings is tolerated up to convergence-related serviceability limit states (Li et al., 2018). The latter are surpassed as soon as the largest measured convergence, in absolute terms, exceeds a specific fraction of the outer diameter of the segmental ring, usually 2%, see (DG/TJ08-2123-2013, 2013; Jiang et al., 2021).[1]

Provided that such a serviceability limit state is reached or surpassed, engineers must select and implement remedial measures (Yuan et al., 2012). Nowadays, two main strategies of remediation are discussed in the literature. The first one refers to the treatment of the ground mass by means of grouting in order to adjust the ground pressure acting on the tunnel lining (Zhang et al., 2018b). The grout may be injected either through holes in the tubbings (Li and Chen, 2012; Zhou et al., 2018; Jin et al., 2018) or through boreholes from the ground surface (Zhu et al., 2019). The second remedial strategy is to strengthen the tunnel linings, e.g. based on filament wound profiles (Liu et al.,

* Corresponding author.
E-mail address: Bernhard.Pichler@tuwien.ac.at (B.L.A. Pichler).

[1] As for convergences computed in design simulations of future tunnels, the limit is 3 ‰ in case of aligned longitudinal joints, and 2 ‰ in case they are misaligned (GB/T51438-2021, 2021).

https://doi.org/10.1016/j.tust.2023.105033
Received 8 September 2021; Received in revised form 22 December 2022; Accepted 2 February 2023
Available online 15 February 2023

2017), steel rings (Liu et al., 2018), steel–concrete composites (Zhang et al., 2019a), or ultra-high performance concrete (Liu et al., 2021).

A graphical representation of the deformed configuration of the tunnel ring provides insight into the structural behavior and facilitates the selection of remedial measures. Nowadays, the current configuration of overly deformed tunnel rings can be documented by means of full-field and high-resolution laser-scanning (Nuttens et al., 2014; Xie and Lu, 2017) and photogrammetry (Ai et al., 2016). However, engineers would even better understand the structural behavior of tunnel rings if the displacement history of an entire tunnel ring could be reconstructed (Li et al., 2017). Such a reconstruction must be based on *available* data from *historic* structural monitoring, mostly in the form of convergences (T/CSPSTC 43-2019, 2019). This is setting the scene for the present contribution.

This study deals with the question whether or not it is possible to reconstruct deformed configurations of segmental tunnel rings based on *two* convergence measurements. For that purpose, a real-scale test of a segmental tunnel ring was analyzed. Structural monitoring included measurement of convergences in *six* different directions. This is beneficial to the present study, because the available experimental data allow for focusing the analysis on the vertical and horizontal convergences and for assessing the quality of the obtained results based on the other four available convergences.

A method for reconstructing the deformed configuration of segmental tunnel rings, based on two measured convergences, is presented. The approach rests on rigid body kinematics. This is motivated as follows: Convergences of segmental tunnel rings are governed by rigid body displacements of the tubbings (Blom, 2002; El Naggar and Hinchberger, 2008). The deformations of the tubbings, resulting from normal forces and bending moments, only produce some 5% of the convergences (Zhang et al., 2019b). This implies that any *deformed* configuration of a segmental lining can be well approximated by means of a kinematic description of the *rigid body* displacements of the tubbings, associated with their relative rotations at the joints. The analyzed segmental ring consists of six tubbings and has three kinematic degrees of freedom. Thus, all possible states of rigid body displacements can be described mathematically as a linear combination of three independent *modes* of rigid body displacements. Because the analyzed tunnel ring is initially *symmetric*, it is possible to introduce *one symmetric* mode (Zhang et al., 2019b) and *two antisymmetric* modes (Jiang et al., 2021). Thus, reconstruction of the deformed configuration based on *two* measured convergences requires the identification of three scalar values, representing components of the three modes of rigid body displacements.

The focus of the present paper is on single rings. This is reasonable for loading scenarios which are characterized by insignificant interaction between adjacent rings, as resulting from (i) small axial loading, (ii) radial loading that is almost uniform in the longitudinal direction, and (iii) adjacent rings with aligned longitudinal joints, see (Zhang et al., 2019c). Liu et al. (2022) investigated ring-to-ring interaction in case of large axial loading and misaligned longitudinal joints of neighboring rings. This interaction was shown to lead to (i) a significant increase of the deformations of the tubbings, resulting from additional normal forces and bending moments, and (ii) a decrease of relative rotations at the joints, associated with rigid body displacements of the tubbings. In such situations, it is possible that the convergences are not only governed by rigid body displacements of the tubbings, but that their deformations also play an important role. If this is the case, the applicability of the present developments is questionable.

The paper is organized as follows. Section 2 contains the convergences measured during a real-scale test of a segmental tunnel ring. Section 3 focuses on the reconstruction of deformed configurations, based on measured vertical and horizontal convergences. This reconstruction rests on the mathematical description of the three modes of rigid body displacements and on an expression for the convergences as a function of the components of these three modes. The proposed method is described and applied to the horizontal and vertical convergences measured in the final state of the test. Finally, the evolution of the deformed configurations of the tubbing ring is traced backwards from the end to the beginning of the test. Section 4 contains the conclusions drawn from the presented study and recommendations for practical applications.

Fig. 1. Real-scale laboratory test of a segmental tunnel ring: photo of the setup.

2. Convergences measured during the test of a real-scale segmental tunnel ring

A real-scale segmental tunnel ring, as is frequently used for metro tunnels in Shanghai, was tested at Tongji University, see Fig. 1. The structure consisted of six tubbings. The six joints in between were located at angular positions

$$\varphi \in \{8°,\ 73°,\ 138°,\ 222°,\ 287°,\ 352°\}, \tag{1}$$

see Fig. 2(a). The radius of the axis of the ring, R, amounted to 2925 mm. The radial thickness of the tubbings, h, was equal to 350 mm. Thus, the outer diameter of the ring is obtained as

$$D_o = 2\,R + h = 6200\,\text{mm}. \tag{2}$$

During testing, the segmental ring was subjected to radial forces imposed by means of 24 hydraulic jacks. They were organized in three groups, see Fig. 2(a). The corresponding point loads are referred to as P_1, P_2, and P_3, see Fig. 2(b) for their intensities as functions of the load steps. The test was carried out in two phases. The first one consisted of nine load steps, associated with and referred to the application of loads simulating the ground pressure. The ratio between vertical and horizontal ground pressure amounted to 0.7. The remaining load steps simulated the decrease of the horizontal ground pressure resulting from excavation in the lateral vicinity of the tunnel.

Convergences were measured in six directions, described by angular coordinates

$$\psi \in \{0°\ ,\ 42°\ ,\ 73°\ ,\ 90°\ ,107°\ ,\ 138°\}, \tag{3}$$

see Fig. 3. Positive values of convergences, $C^{exp}(\psi) > 0$, refer to an increase of the distance between two opposite measurement points, negative values, $C^{exp}(\psi) < 0$, to a decrease. Notably, both φ and ψ are equivalent angular coordinates with the origin at the crown of the segmental tunnel ring. The reason for introducing two *different* symbols for *the same* coordinate is to render the presentation as clear as possible. φ_j denotes the position of the j^{th} joint between neighboring tubbings, and ψ_k refers to the direction of the k^{th} available convergence measurement.

During the first phase of the test, see load steps 1 to 9, the convergences increased rather moderately and virtually linearly, see Fig. 3. During the second phase, the convergences increased significantly,

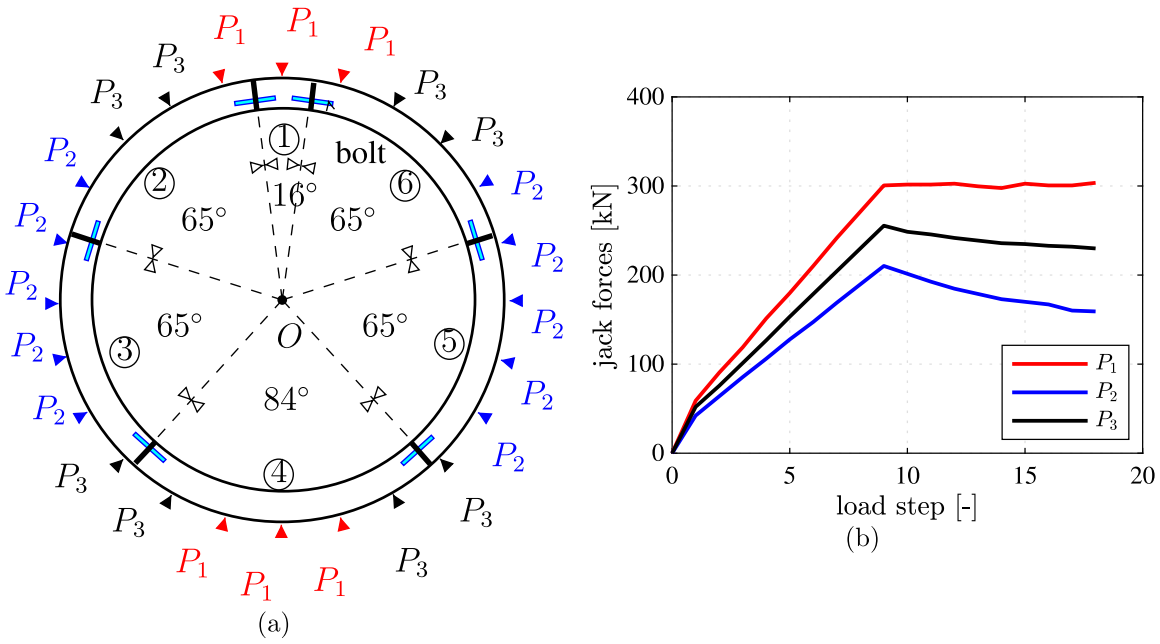

Fig. 2. Real-scale testing of a segmental tunnel ring: (a) arrangement of the tubbings and the hydraulic jacks, (b) prescribed intensities of the jack forces.

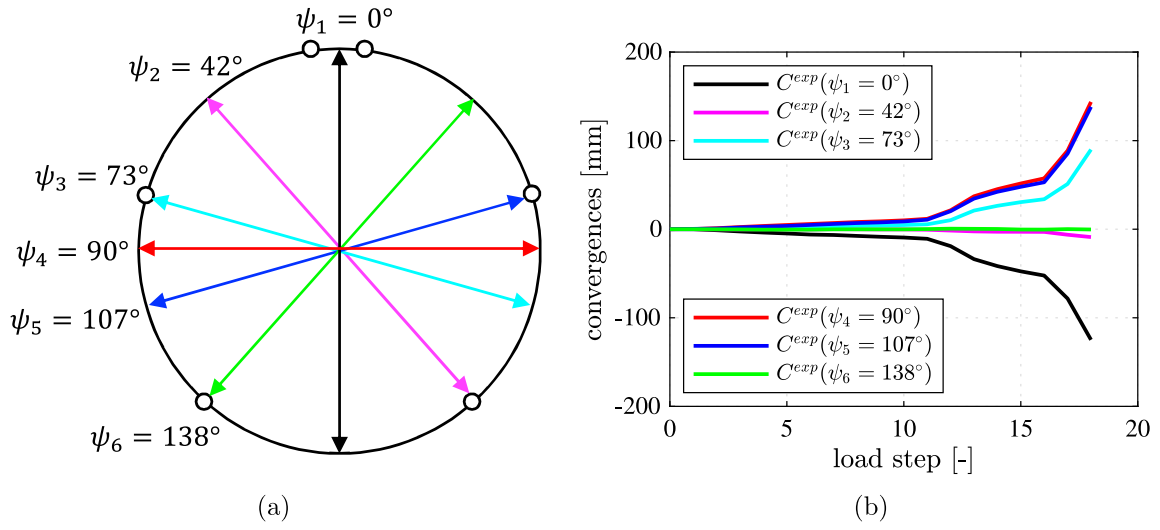

Fig. 3. Results from structural monitoring during real-scale testing: (a) specific directions of measured convergences, (b) measured convergences: negative values refer to a decrease of the initial diameter, positive values to an increase.

except in the directions of $\psi_2 = 42°$ and $\psi_6 = 138°$. The test was stopped at load step 18, because a convergence-related serviceability limit state had been surpassed, given that the absolute value of the largest measured convergence, $C(\psi_4 = 90°) = +144\,\text{mm}$, exceeded 2% of the outer diameter of the structure, see Eq. (2).

3. Reconstruction of the deformed configurations based on measured convergences

3.1. Mathematical description of rigid body displacements associated with relative rotations at the joints (Jiang et al., 2021)

Convergences are governed by rigid body displacements of the tubbings (Blom, 2002; El Naggar and Hinchberger, 2008), while deformations of the tubbings only produce some 5% of the convergences (Zhang et al., 2019b). Rigid body displacements of a segmental tunnel ring, expressed as functions of the relative rotations at the joints, read as (Jiang et al., 2021)

$$u(\varphi) = \sum_{j=1}^{6} R\Delta\theta_j \sin(\varphi - \varphi_j) H(\varphi - \varphi_j), \tag{4}$$

$$v(\varphi) = -\sum_{j=1}^{6} R\Delta\theta_j \left[1 - \cos(\varphi - \varphi_j)\right] H(\varphi - \varphi_j), \tag{5}$$

$$\theta(\varphi) = \sum_{j=1}^{6} \Delta\theta_j H(\varphi - \varphi_j), \tag{6}$$

where u and v denote the radial and tangential displacement component, respectively, whereas θ and $\Delta\theta_j$ stand for the rotation of the cross-section and the relative rotation at the j^{th} joint, respectively, and $H(\varphi - \varphi_j)$ denotes the Heaviside function. Notably derivation of Eqs. (4)–(6) is based on the transfer relations (Zhang et al., 2017), representing analytical solutions of the linear theory of thin circular arches, presented in the Appendix A. Because segmental tunnel linings are *closed* rings, the relative rotations must satisfy the following

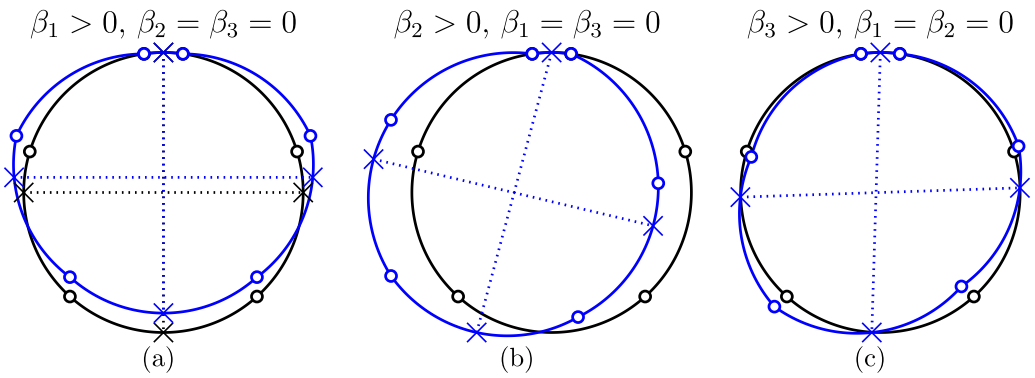

Fig. 4. Three modes of rigid-body displacements of the analyzed segmental ring: (a) symmetric mode, see the first column of $\boldsymbol{A}$ in Eq. (10), (b) the first antisymmetric mode, see the second column of $\boldsymbol{A}$ in Eq. (10), and (c) the second antisymmetric mode, see the third column of $\boldsymbol{A}$ in Eq. (10); crosses mark the points located at 0°, 90°, 180°, and 270°; after (Jiang et al., 2021).

continuity conditions (Jiang et al., 2021)

$$u(0) = u(2\pi) \Rightarrow \sum_{j=1}^{6} \Delta\theta_j \sin\varphi_j = 0\,, \tag{7}$$

$$v(0) = v(2\pi) \Rightarrow \sum_{j=1}^{6} \Delta\theta_j (1 - \cos\varphi_j) = 0\,, \tag{8}$$

$$\theta(0) = \theta(2\pi) \Rightarrow \sum_{j=1}^{6} \Delta\theta_j = 0\,. \tag{9}$$

Because *six* relative rotations must satisfy *three* continuity conditions, there are infinitely many solutions. They can be described mathematically as the superposition of three linearly independent modes of rigid body displacements. As for the analyzed *symmetric* ring, it is possible to introduce one symmetric and two antisymmetric modes of rigid body displacements, see Fig. 4. Thus, the relative rotations can be expressed as (Jiang et al., 2021):

$$\underbrace{\begin{bmatrix} \Delta\theta_1 \\ \Delta\theta_2 \\ \Delta\theta_3 \\ \Delta\theta_4 \\ \Delta\theta_5 \\ \Delta\theta_6 \end{bmatrix}}_{\boldsymbol{\Delta\theta}} = \underbrace{\begin{bmatrix} +0.3427 & +0.6923 & -0.1171 \\ -0.5737 & \pm 0.0000 & +0.4111 \\ +0.2310 & -0.1440 & -0.5632 \\ +0.2310 & +0.1440 & +0.5632 \\ -0.5737 & \mp 0.0000 & -0.4111 \\ +0.3427 & -0.6923 & +0.1171 \end{bmatrix}}_{\boldsymbol{A}} \cdot \underbrace{\begin{bmatrix} \beta_1 \\ \beta_2 \\ \beta_3 \end{bmatrix}}_{\boldsymbol{\beta}}. \tag{10}$$

In Eq. (10), β_1 is the component associated with the symmetric mode of rigid body displacements, see the first column of $\boldsymbol{A}$ and Fig. 4(a). β_2 is the component associated with the first antisymmetric mode, see the second column of $\boldsymbol{A}$ and Fig. 4(b). β_3 is associated with the second antisymmetric mode, see the third column of $\boldsymbol{A}$ and Fig. 4(c).

The base matrix $\boldsymbol{A}$ in Eq. (10) is customized for the tunnel ring shown in Fig. 2(a), with positions of the joints according to Eq. (1). As for other segmental tunnel rings, the base matrix $\boldsymbol{A}$ can be derived, following the approach presented in Appendix B.

3.2. Convergences as function of the components associated with the three modes of rigid body displacements

Identification of the deformed configuration of a segmental tunnel ring based on measured convergences requires an expression for the convergence in the ψ_k-direction, $C(\psi_k)$, as a function of β_1, β_2, and β_3. To this end, $C(\psi_k)$ is related by means of the Pythagorean theorem to the displacement components $u(\psi_k)$ and $v(\psi_k)$ as well as $u(\psi_k + \pi)$ and $v(\psi_k + \pi)$, see also Fig. 5:

$$\Big[2R + u(\psi_k) + u(\psi_k + \pi)\Big]^2 + \Big[v(\psi_k) + v(\psi_k + \pi)\Big]^2 = \Big[2R + C(\psi_k)\Big]^2. \tag{11}$$

Insertion of the relative rotations according to Eq. (10) into Eqs. (4) and (5) and of the resulting expressions into Eq. (11) yields, after

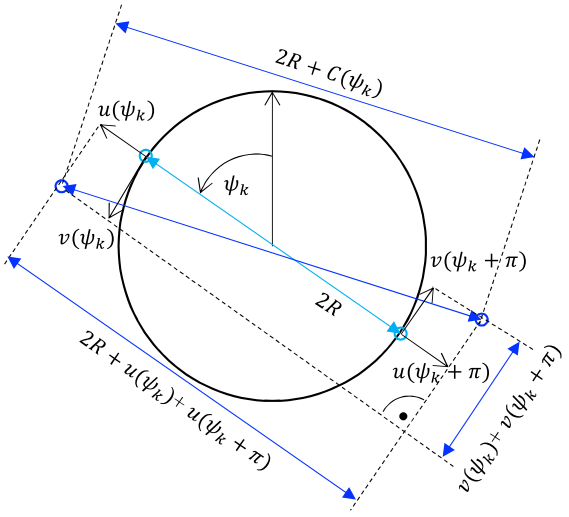

Fig. 5. Relation between the convergence in the ψ_k direction, $C(\psi_k)$, and the displacement components $u(\psi_k)$ and $v(\psi_k)$ as well as $u(\psi_k + \pi)$ and $v(\psi_k + \pi)$.

having solved for $C(\psi_k)$, the sought expression for the convergence in the ψ_k-direction as a function of β_1, β_2, and β_3:

$$\begin{aligned} C(\psi_k; \beta_1, \beta_2, \beta_3) = \Bigg\{ \Bigg[2R + \sum_{j=1}^{6} R\Big(A_{j,1}\,\beta_1 + A_{j,2}\,\beta_2 + A_{j,3}\,\beta_3\Big) \times \\ \Big\{ \sin(\psi_k - \varphi_j) H(\psi_k - \varphi_j) + \sin(\psi_k + \pi - \varphi_j) H(\psi_k + \pi - \varphi_j) \Big\} \Bigg]^2 + \\ \Bigg[\sum_{j=1}^{6} R\Big(A_{j,1}\,\beta_1 + A_{j,2}\,\beta_2 + A_{j,3}\,\beta_3\Big) \Big\{ \big[1 - \cos(\psi_k - \varphi_j)\big] H(\psi_k - \varphi_j) + \\ \big[1 - \cos(\psi_k + \pi - \varphi_j)\big] H(\psi_k + \pi - \varphi_j) \Big\} \Bigg]^2 \Bigg\}^{\frac{1}{2}} - 2R\,. \end{aligned} \tag{12}$$

The mathematical problem, dealt with in the following Subsections, refers to the identification of optimal values of the components of the rigid body displacement, β_1, β_2, and β_3, such that the modeled convergences according to Eq. (12) reproduce the corresponding measurements.

3.3. Reconstruction of the deformed configuration of the tunnel ring based on horizontal and vertical convergences measured in the final state of the test

Measurements of convergences of segmental linings must be carried out in a minimum-invasive fashion in order to disturb the operation of

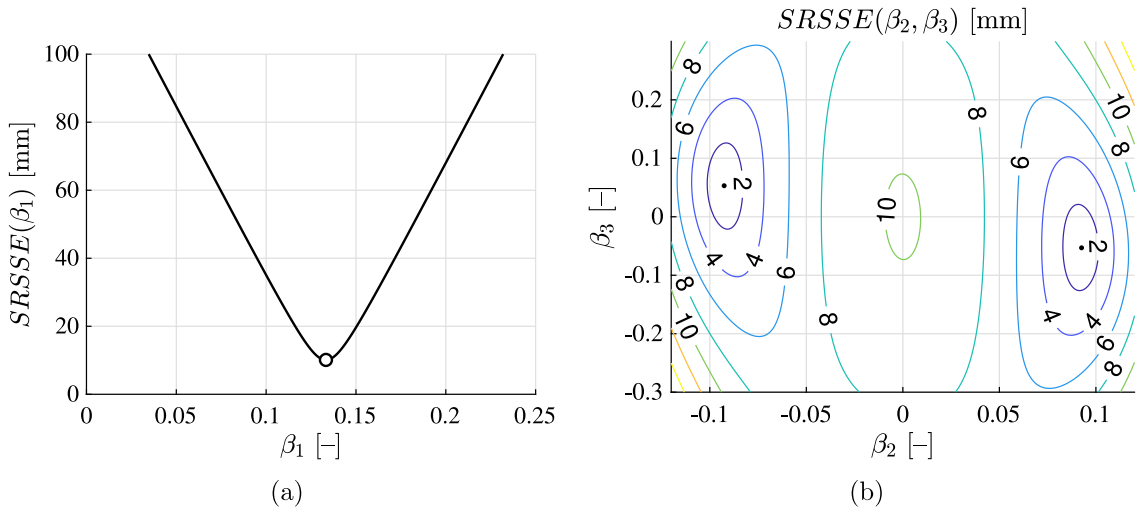

Fig. 6. Optimization of β_1, β_2, and β_3 in order to reproduce the vertical and horizontal convergences measured at load step 18 (= beyond the serviceability limit state): (a) optimization of β_1 according to Eq. (14), see also Eq. (15), and (b) optimization of β_2 and β_3 according to Eq. (16), see also Eqs. (17) and (18).

tunnels as little as possible. Therefore, convergences are usually measured in selected cross-sections and in two directions only. In order to simulate such a practical scenario, the first analysis of the experimental data of Section 2 is limited to vertical ($\psi_1 = 0$) and horizontal ($\psi_4 = \pi/2$) convergences. In order to check whether or not reconstruction of the deformed configuration based on two convergences is possible, the first analysis is restricted to load step 18, at which a convergence-related serviceability limit state has been surpassed, see Section 2. The measured convergences in vertical and horizontal direction read as $C^{exp}(\psi_1) = -125\,\text{mm}$ and $C^{exp}(\psi_4) = +144\,\text{mm}$, respectively, see also Fig. 3(b).

The values of the *three* optimization variables, β_1, β_2, and β_3, are to be identified such that the vertical and horizontal convergences, modeled according to Eq. (12), reproduce the *two* measured values. Thus, the square root of the sum of squared errors ($SRSSE$) between measured and modeled convergences must vanish:

$$SRSSE(\beta_1,\beta_2,\beta_3) = \sqrt{\frac{1}{2}\sum_{k=1,4}\left[C^{exp}(\psi_k) - C(\psi_k,\beta_1,\beta_2,\beta_3)\right]^2} = 0\,. \tag{13}$$

This optimization problem is under-determined. As a remedy, it will be assumed that the deformed configuration is governed by symmetric rigid body displacements. The identification of β_1, β_2, and β_3 will be organized in two steps. At first, β_2 and β_3 will be set equal to zero, and β_1 will be identified such as to explain the two convergences in the best-possible fashion. In step 2, the remaining differences between modeled and measured convergences will be reduced to zero, based on suitably identified values of β_2 and β_3. These two steps will be described in more detail in the following two paragraphs.

Step 1 is limited to *symmetric* rigid body displacements. Accordingly, the antisymmetric components β_2 and β_3 are set equal to zero. β_1 is identified such as to minimize the square root of the sum of squared errors:

$$SRSSE(\beta_1) = \sqrt{\frac{1}{2}\sum_{k=1,4}\left[C^{exp}(\psi_k) - C(\psi_k,\beta_1,\beta_2=0,\beta_3=0)\right]^2} \to \text{min.} \tag{14}$$

The solution of Eq. (14) is computed numerically and reads as:

$$\beta_1 = 0.1333\,, \tag{15}$$

see Fig. 6(a). The related value of $SRSSE$ according to Eq. (14) amounts to 10.1 mm. The modeled vertical and horizontal convergences read as $C(\psi_1) = -135.1\,\text{mm}$ and $C(\psi_4) = +133.9\,\text{mm}$, respectively.

Table 1
Complete set of six convergences measured at load step 18, see also Eq. (3) and Fig. 3(b).

$\psi_1 = 0.0000\,\text{rad}$	$C^{exp}(\psi_1) = -125\,\text{mm}$
$\psi_2 = 0.7330\,\text{rad}$	$C^{exp}(\psi_2) = -9\,\text{mm}$
$\psi_3 = 1.2741\,\text{rad}$	$C^{exp}(\psi_3) = +90\,\text{mm}$
$\psi_4 = 1.5708\,\text{rad}$	$C^{exp}(\psi_4) = +144\,\text{mm}$
$\psi_5 = 1.8675\,\text{rad}$	$C^{exp}(\psi_5) = +138\,\text{mm}$
$\psi_6 = 2.4086\,\text{rad}$	$C^{exp}(\psi_6) = \pm 0\,\text{mm}$

Step 2 focuses on identifying the *antisymmetric* components of rigid body displacements in order to reduce the remaining differences between the measured and the modeled convergences to zero. In mathematical terms, this problem reads as

$$SRSSE(\beta_2,\beta_3) = \sqrt{\frac{1}{2}\sum_{k=1,4}\left[C^{exp}(\psi_k) - C(\psi_k,\beta_1=0.1333,\beta_2,\beta_3)\right]^2} = 0\,. \tag{16}$$

Eq. (16) is solved numerically, see Fig. 6(b). Two solutions are obtained:

$$\beta_{1a} = +0.1331\,,\ \beta_{2a} = -0.09258\,,\ \beta_{3a} = +0.05308\,, \tag{17}$$

$$\beta_{1b} = +0.1331\,,\ \beta_{2b} = +0.09258\,,\ \beta_{3b} = -0.05308\,. \tag{18}$$

In order to assess the quality of these two solutions, the error of reproduction of *all six* convergences is computed:

$$SRSSE(\beta_{1a},\beta_{2a},\beta_{3a}) = \sqrt{\frac{1}{6}\sum_{k=1}^{6}\left[C^{exp}(\psi_k) - C(\psi_k,\beta_{1a},\beta_{2a},\beta_{3a})\right]^2} = 16.4\,\text{mm}, \tag{19}$$

$$SRSSE(\beta_{1b},\beta_{2b},\beta_{3b}) = \sqrt{\frac{1}{6}\sum_{k=1}^{6}\left[C^{exp}(\psi_k) - C(\psi_k,\beta_{1b},\beta_{2b},\beta_{3b})\right]^2} = 29.5\,\text{mm}, \tag{20}$$

see also Table 1. These results underline that the solution (17) reproduces all six measured convergences better than the solution (18), see also Fig. 7.

The respective deformed configurations are obtained by inserting the solutions (17) and (18), respectively, into Eq. (10), and the obtained relative rotations into Eqs. (4) and (5), see the red and the green graph in Fig. 8(a) and (b). The two solutions are mirror images with respect to a vertical axis of symmetry.

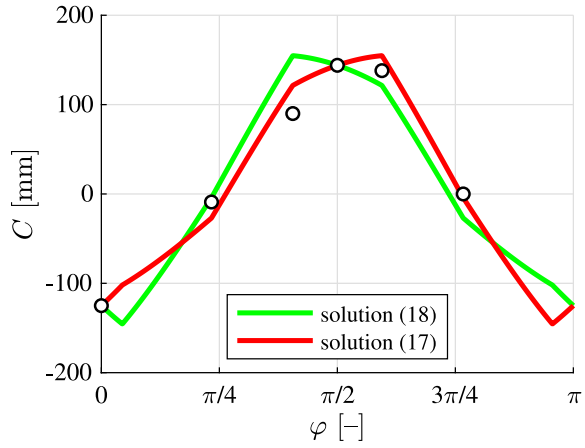

Fig. 7. Convergence as a function of the angular coordinate φ: comparison of measured convergences, see the circles, with identified results, reproducing the vertical and horizontal convergences.

For comparison, also the deformed configuration obtained by Jiang et al. (2021) is included in Fig. 8, see the blue graphs. It was obtained as the result of a comprehensive structural analysis accounting for the relative rotations at the joints *and* the prescribed point loads. Thus, the computed displacements account for the deformations of the tubbings: contraction in the tangential direction produced by compressive normal forces and changes of curvature produced by bending moments. The relative rotations at the joints were first estimated based on tangential displacement jumps, measured at the inner and outer gaps of the joints. Subsequently, they were postprocessed in order to explain the measured horizontal and vertical convergences in the best-possible fashion.

The deformed configuration of the tested ring according to Eqs. (17), (10), (4), and (5), see the red graph in Fig. 8(a), is virtually identical with the deformed configuration taken from (Jiang et al., 2021), see the blue graph in Fig. 8(a). This underlines the fact that the deformations of the tubbings, resulting from normal forces and bending moments, do not contribute significantly to the convergences.

3.4. Reconstruction of the deformed configuration of the tunnel ring based on all six convergences measured in the final state of the test

In order to further demonstrate the quality of the reproduction of the measured convergences by the solution (17), identification of β_1, β_2, and β_3 is repeated, this time, however, based on *all six* convergences measured at load step 18, see Table 1. This optimization problem is over-determined. Therefore, β_1, β_2, and β_3 are identified such as to minimize the sum of the squared errors between the six pairs of measured and modeled convergences:

$$SRSSE(\beta_1,\beta_2,\beta_3)=\sqrt{\frac{1}{6}\sum_{k=1}^{6}\left[C^{exp}(\psi_k)-C(\psi_k,\beta_1,\beta_2,\beta_3)\right]^2}\rightarrow \min. \quad (21)$$

The solution is obtained numerically. It reads as

$$\beta_{1c}=+0.1205\,,\quad \beta_{2c}=-0.09331\,,\quad \beta_{3c}=+0.05145\,. \quad (22)$$

The modeled convergences agree well with the available experimental measurements, see Fig. 9(a).

The related value of $SRSSE$ according to Eq. (21) amounts to

$$SRSSE(\beta_{1c},\beta_{2c},\beta_{3c})=\sqrt{\frac{1}{6}\sum_{k=1}^{6}\left[C^{exp}(\psi_k)-C(\psi_k,\beta_{1c},\beta_{2c},\beta_{3c})\right]^2}=12.6\,\text{mm}. \quad (23)$$

This result is slightly better than that based on the vertical and horizontal convergences, compare Eq. (23) with Eq. (19). Still, the deformed configuration corresponding to the solution (22) is virtually identical with the one corresponding to the solution (17), see Fig. 9(b). This corroborates the robustness of the presented approach for determination of rigid body displacements of a segmental tunnel ring based on vertical and horizontal convergences.

3.5. Backwards tracing of the evolution of the deformed configuration, starting from the final state of the test

It remains to be checked whether or not the evolution of the deformed configuration can be traced backwards, from load step 18 to the period of time before the segmental tunnel ring has surpassed the serviceability limit state. To this end, the deformed configuration is reconstructed, load step by load step, in descending order: 17, 16, 15, … , 1.

Sets of values of β_1, β_2, and β_3 are computed twice for every load step, using the method based on vertical and horizontal convergences, see Section 3.3, and the one based on all six available convergence measurements, see Section 3.4. The optimization problems (14), (16), and (21) are solved numerically in the vicinity of the solution for the previously analyzed load step, see Fig. 10 for the results. The solid lines refer to the method based on vertical and horizontal convergences, whereas the dashed lines refers to the method based on all six measured convergences. Their very good agreement proves that the approach based on the vertical and horizontal convergences is capable of identifying deformed configurations of segmental tunnel rings.

3.6. Deformed configurations in different classes of convergence-related serviceability

Current Chinese codes of practice, see e.g. DG/TJ08-2123-2013 (2013), define four classes of convergence-related serviceability of segmental tunnel rings. This classification is based on the largest measured convergence, in absolute terms, i.e.

$$C_{max}=\max\{|C_v|,\ |C_h|\}\,, \quad (24)$$

where $C_v = C(\psi_1)$ and $C_h = C(\psi_4)$ denote the vertical and the horizontal convergences, respectively. Class A, “acceptable serviceability”, is defined as $C_{max} \le 0.008\,D_o$, class B, “reduced serviceability”, as $0.008\,D_o < C_{max} \le 0.012\,D_o$, class C, “endangered serviceability”, as $0.012\,D_o < C_{max} \le 0.020\,D_o$, and class D, “violated serviceability”, as $C_{max} > 0.020\,D_o$, see also the top of Fig. 10. In order to illustrate deformed configurations, representative of these four classes, the focus is placed on load steps 12, 16, 17, and 18, see Fig. 10. Deformed configurations are computed from the β-values illustrated in Fig. 10, based on Eqs. (10), (4), and (5). A sequence of deformed configurations is obtained. It illustrates the evolution of the state of displacements of the segmental ring throughout its loading history, leading to the configuration at which the serviceability limit state has been surpassed, see Fig. 11.

The displacements are qualitatively similar. Because of their continuous growth, the segmental tunnel ring is passing though all classes of convergence-related serviceability. This underlines that the unsymmetric structural behavior has developed continuously rather than having been caused by singular events such as sudden local damage of specific parts of the ring.

4. Conclusions and recommendations

The presented study has confirmed that convergences of segmental tunnel rings are governed by rigid body displacements of the tubbings, because their deformations, resulting from normal forces and bending moments, do not contribute significantly to the overall state of displacements of segmental tunnel rings. This is the basis for the first set of conclusions:

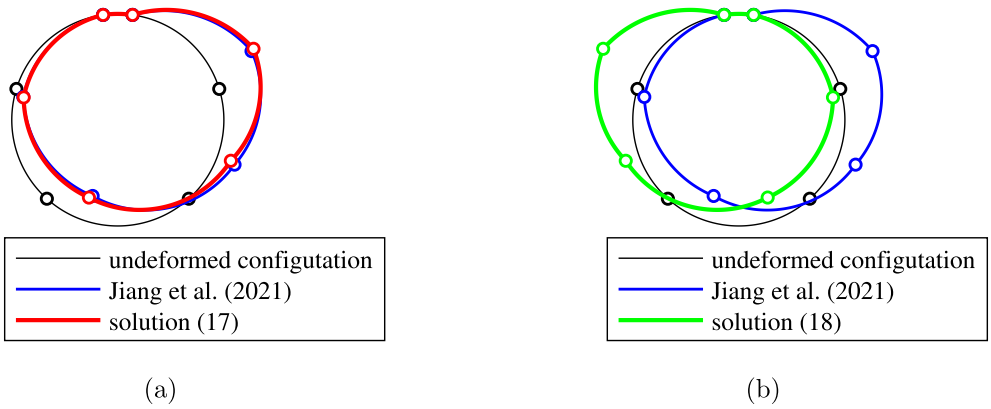

Fig. 8. Deformed configurations of the tested ring at load step 18 according to (a) Eq. (17), see the red graph, and (b) Eq. (18), see the green graph, and comparison with the hybrid solution obtained by Jiang et al. (2021), who have used the point loads of load step 18, the measured relative rotations at the joints, and the measured vertical and horizontal convergences as input for hybrid structural analysis accounting for the deformation of the tubbings, see the blue graphs.

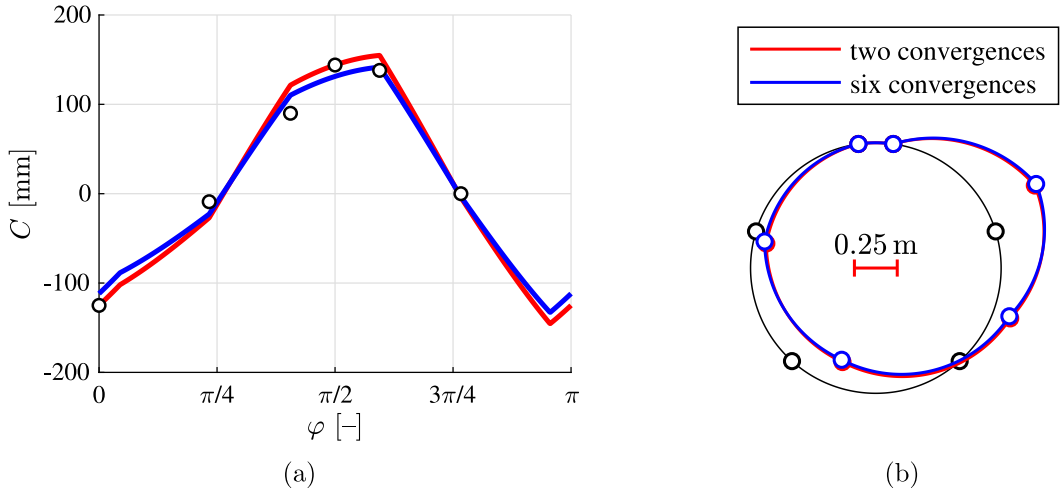

Fig. 9. (a) Convergence as a function of the angular coordinate φ: comparison of measured convergences, see the rings, with results identified by reproducing the vertical and horizontal convergences, see the red graph and Eq. (17), as well as with results identified by reproducing all six measured convergences in the best-possible fashion, see the blue graph and Eq. (22), and (b) comparison of deformed configurations obtained by means of two measured convergences, see Eq. (17) and the red graph, and six measured convergences, see Eq. (22) and the blue graph.

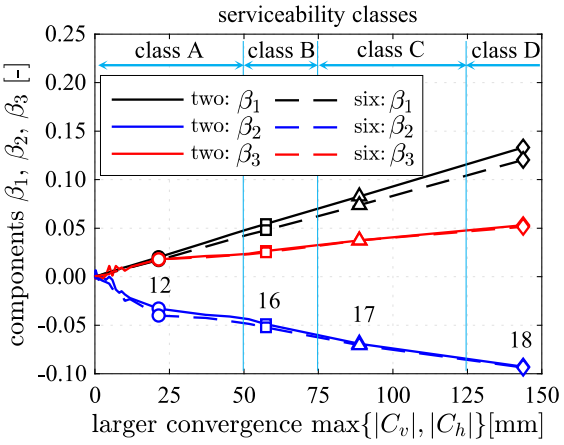

Fig. 10. Evolution of the rigid body displacement components β_1, β_2, and β_3, as a function of the larger convergence, $\max\{|C_v|, |C_h|\}$; solid lines refer to the method based on vertical and horizontal convergences, whereas the dashed lines refer to the method based on all six measured convergences.

- *Deformed* configurations of a segmental lining can be well approximated based on the kinematics of *rigid body* displacements of the tubbings, resulting from relative rotations at the joints.
- Segmental rings, consisting of n tubbings, have n joints and $n-3$ kinematic degrees of freedom. All possible states of rigid body displacements can be described mathematically as linear combinations of $n-3$ linearly independent modes of rigid body displacements.
- Deformed configurations of a segmental tunnel ring can be described by means of $n-3$ scalar values, representing components of the $n-3$ linearly independent modes of rigid body displacements.
- Even if a segmental tunnel ring is initially *symmetric*, also *antisymmetric* modes of rigid body displacements may arise.

The analyzed ring is symmetric and consists of six tubbings. Thus, it has *one* symmetric and *two* antisymmetric modes of rigid body displacements, see Fig. 4. The related components are denoted as β_1, β_2, and β_3. The line of arguments in the bulleted list above has provided the motivation to develop a method which allows for identification of β_1, β_2, and β_3, based on two measured convergences. It is recommended to solve this under-determined optimization problem in two steps:

Step 1: Assuming that the symmetric mode of rigid body displacements governs the deformed configuration, β_1 is optimized

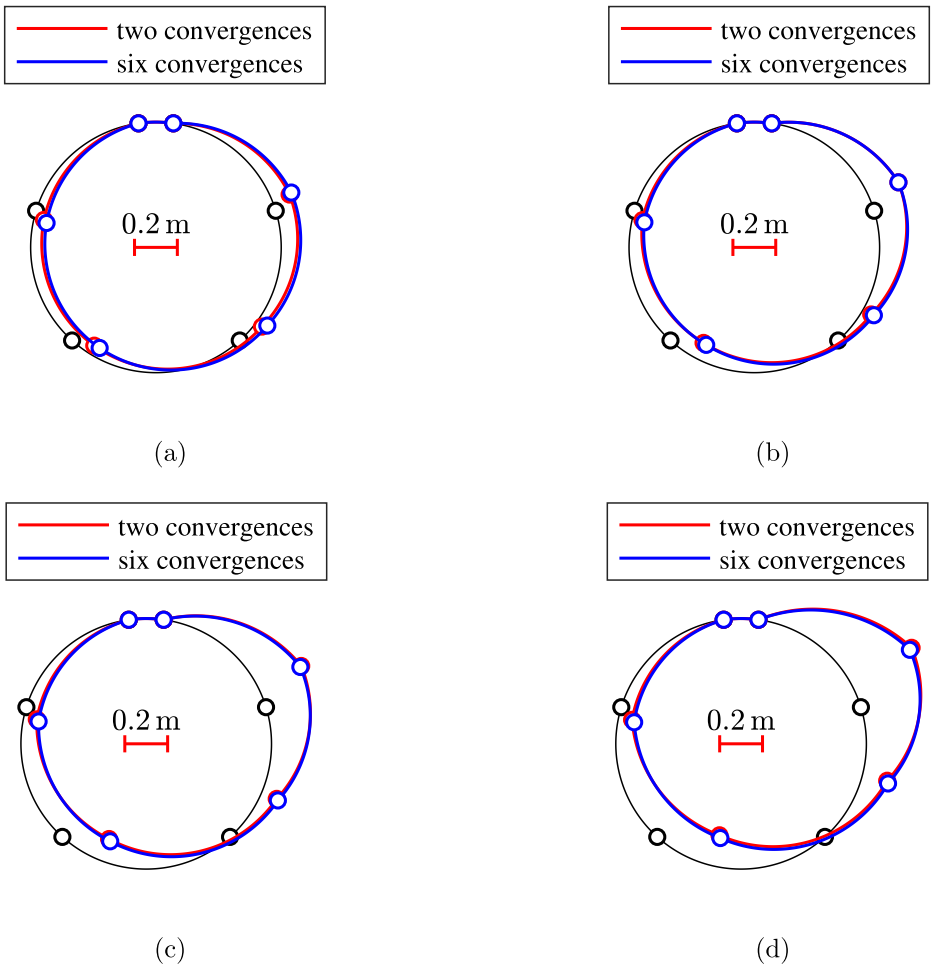

Fig. 11. Deformed configurations, identified by means of vertical and horizontal convergences, see the red graphs, and with the help of all six measured convergences, see the blue graphs: (a) load step 12 in serviceability class A, "acceptable serviceability", (b) load step 16 in serviceability class B, "reduced serviceability", (c) load step 17 in serviceability class C, "endangered serviceability", and (d) load step 18 in serviceability class D, "violated serviceability".

in order to reproduce the two measured convergences in the best-possible fashion, while β_2 and β_3 are set equal to zero.

Step 2: The remaining differences between measured and modeled convergences are reduced to zero, based on the antisymmetric modes of rigid body displacements, i.e. by means of optimization of β_2 and β_3, while β_1 is kept constant at the value identified in the first step.

Step 2 has resulted in two axisymmetric solutions, see Fig. 8. This has raised the need to identify the solution which is more realistic. Therefore, it is recommended to organize the reproduction of the displacement history of segmental tunnel rings throughout the monitoring period during which convergences were measured, as follows.

- The analysis starts at the *current* configuration of the tunnel ring. In order to identify the more realistic solution for β_1, β_2, and β_3, it is recommended to measure convergences in several directions: the more of them, the better.
- The values obtained for β_1, β_2, and β_3 are the basis for the analysis of the evolution of the deformed configuration, based on past convergence measurements, even if these monitoring data refer to two directions only.
- Retrogressing step-by-step in time, the values of β_1, β_2, and β_3 are optimized, using the previously described two-step procedure. As for the numerical solution of the optimization problem regarding β_2 and β_3, see Step 2, the solution of the previously analyzed configuration is used as the starting point.

This procedure was applied to a segmental tunnel ring, which was tested until the convergence-related serviceability limit state had been surpassed. Results obtained by means of measured vertical and horizontal convergences could be shown to be reliable, because the convergences were measured in six directions during the well-instrumented test. The success of the method is remarkable, because the tested structure has clearly shown an unsymmetric behavior, challenging the assumption used in Step 1, see above.

Based on data from real-scale testing of a segmental tunnel ring, it was shown that the presented method is useful for engineering applications, because it allows for translating measured histories of two convergences into a sequence of images, visualizing the evolution of the displacements of the *entire* tunnel ring (see, e.g., Fig. 11). Such a sequence of images provides much better insight into the structural behavior of the tunnel lining than diagrams showing the evolution of *single* convergences (see, e.g., Fig. 3). Therefore, the presented method is appreciated by tunnel engineers, striving to understand the structural behavior of segmental linings throughout their monitored history. It is of particular significance for engineering practice that the presented method is capable of coping with very challenging scenarios, characterized by convergences which have grown so large that tunnel serviceability is at stake. It is concluded that the developed approach is a very effective enrichment of the pool of methods available to support the decision making process regarding remedial measures for segmental tunnel linings, the serviceability of which is endangered or even violated by large convergences.

The presented study is a successful example for application-oriented research in the engineering sciences. The motivation was provided by an unsolved problem in tunneling practice. Research was based on scientifically well-rooted theoretical concepts. The developed method has a high degree of novelty. It is only as complex as necessary to provide a solution to the problem at hand. At the same time, it is as simple as possible to ensure that it will be used in the engineering practice. The method was systematically verified, because it survived a strictly quantitative attempt of falsification. This test of the method was severe, because it was based on high-quality monitoring data, recorded during real-scale testing of a segmental tunnel ring. This underlines that the developed method is very well suited for applications with data from real tunnels. This is the logic next step, representing an interesting topic for follow-up work.

Finally, it is emphasized that the presented developments are based on the assumption that convergences are governed by rigid body displacements of the segments, resulting from relative rotations at the joints. This assumption was shown to be reasonable for the analysis of a single-ring laboratory test. As for tunnel linings with significant ring-to-ring interaction, this assumption must be scrutinized.

CRediT authorship contribution statement

Jiao-Long Zhang: Methodology, Software, Writing – original draft. **Zijie Jiang:** Validation, Investigation. **Xian Liu:** Data curation, Investigation. **Yong Yuan:** Supervision, Funding acquisition. **Herbert A. Mang:** Writing - review & editing. **Bernhard L.A. Pichler:** Conceptualization, Methodology, Supervision, Software, Writing – review & editing.

Declaration of competing interest

The authors declare that they have no known competing financial interests or personal relationships that could have appeared to influence the work reported in this paper.

Data availability

Data will be made available on request.

Acknowledgments

Financial support by the National Key Research and Development Program of China (Grant No. 2021YFE0114100), the National Natural Science Foundation of China (Grant No. 51908424 and U1934210), and by the Shanghai Rising-Star Program, China (No. 22QB1405000) is gratefully acknowledged. The authors are indebted to Prof. Xupeng Yao, Dr. Yumeng Zhang, Mr. Qihao Sun, and Mr. Yimin Qin from Tongji University for many helpful discussions. In addition, the authors acknowledge TU Wien Bibliothek for financial support through its Open Access Funding Programme.

Appendix A. Transfer relations of the linear theory of thin circular arches

Transfer relations, representing analytical solutions of the linear theory of thin circular arches, are given as (Zhang et al., 2017)

$$\begin{bmatrix} u(\varphi) \\ v(\varphi) \\ \theta(\varphi) \\ M(\varphi) \\ N(\varphi) \\ V(\varphi) \\ \hline 1 \end{bmatrix} = \left[\begin{array}{cccccc|c} \cos\varphi & \sin\varphi & T_{13}(\varphi) & T_{14}(\varphi) & T_{15}(\varphi) & T_{16}(\varphi) & \sum u^L(\varphi) \\ -\sin\varphi & \cos\varphi & T_{23}(\varphi) & T_{24}(\varphi) & T_{25}(\varphi) & T_{26}(\varphi) & \sum v^L(\varphi) \\ 0 & 0 & 1 & T_{34}(\varphi) & T_{35}(\varphi) & T_{36}(\varphi) & \sum \theta^L(\varphi) \\ 0 & 0 & 0 & 1 & T_{45}(\varphi) & T_{46}(\varphi) & \sum M^L(\varphi) \\ 0 & 0 & 0 & 0 & \cos\varphi & -\sin\varphi & \sum N^L(\varphi) \\ 0 & 0 & 0 & 0 & \sin\varphi & \cos\varphi & \sum V^L(\varphi) \\ \hline 0 & 0 & 0 & 0 & 0 & 0 & 1 \end{array}\right] \begin{bmatrix} u_i \\ v_i \\ \theta_i \\ M_i \\ N_i \\ V_i \\ \hline 1 \end{bmatrix}, \tag{A.1}$$

where

$$\begin{aligned} &T_{13}(\varphi) = R\ \sin\varphi\,, \quad T_{14}(\varphi) = \frac{R^2}{EI}(\cos\varphi - 1)\,, \\ &T_{15}(\varphi) = \frac{R}{EA}\frac{1}{2}\varphi\sin\varphi + \frac{R^3}{EI}\left(\frac{1}{2}\varphi\sin\varphi + \cos\varphi - 1\right), \\ &T_{16}(\varphi) = \frac{R}{EA}\left(\frac{1}{2}\varphi\cos\varphi - \frac{1}{2}\sin\varphi\right) + \frac{R^3}{EI}\left(\frac{1}{2}\varphi\cos\varphi - \frac{1}{2}\sin\varphi\right), \\ &T_{23}(\varphi) = R\ (\cos\varphi - 1)\,, \quad T_{24}(\varphi) = \frac{R^2}{EI}(\varphi - \sin\varphi)\,, \\ &T_{25}(\varphi) = \frac{R}{EA}\left(\frac{1}{2}\varphi\cos\varphi + \frac{1}{2}\sin\varphi\right) + \frac{R^3}{EI}\left(\varphi - \frac{3}{2}\sin\varphi + \frac{1}{2}\varphi\cos\varphi\right), \\ &T_{26}(\varphi) = \frac{R}{EA}\left(-\frac{1}{2}\varphi\sin\varphi\right) + \frac{R^3}{EI}\left(1 - \cos\varphi - \frac{1}{2}\varphi\sin\varphi\right), \\ &T_{34}(\varphi) = -\frac{R}{EI}\varphi\,, \quad T_{35}(\varphi) = \frac{R^2}{EI}(\sin\varphi - \varphi)\,, \quad T_{36}(\varphi) = \frac{R^2}{EI}(\cos\varphi - 1)\,, \\ &T_{45}(\varphi) = R\ (1 - \cos\varphi)\,, \quad T_{46}(\varphi) = R\ \sin\varphi\,. \end{aligned} \tag{A.2}$$

The vector on the left-hand side of Eq. (A.1) contains the kinematic and the static variables at an arbitrary cross-section, defined by the angular coordinate φ, i.e. the cross-sectional rotation θ, the radial and the tangential displacement, u and v, respectively, the normal force N, the shear force V, and the bending moment M. The matrix on the right-hand side is the so-called transfer matrix. Its top-left six-by-six submatrix refers to the solution for an unloaded part of the arch. The mathematical expressions for the nonzero elements T_{ij} of this submatrix are given in Eq. (A.2). The first six elements in the last column of the transfer matrix in Eq. (A.1) refer to the superposition of solutions for different types of loading. They are available for dead load, interfacial discontinuities of kinematic variables, and point loads (Zhang et al., 2017), a uniform temperature change (Zhang et al., 2018a), ground pressure (Zhang et al., 2019c), and overload on the ground surface (Zhang et al., 2021). In Eq. (A.1), the rightmost vector contains the kinematic and static variables at the initial cross-section $\varphi = 0$ (index "i") . Representing integration constants, they must be identified by means of boundary conditions.

The kinematic quantities, u_i, v_i, and θ_i, refer to rigid body displacements of the entire ring, *without* relative rotations of the tubbings. Given the present focus on convergences, representing relative rather than absolute displacements, they are set equal to zero (Zhang et al., 2017):

$$u_i = v_i = \theta_i = 0\,. \tag{A.3}$$

The static quantities, M_i, N_i, and V_i, are determined by formulating three continuity conditions of a closed ring (Zhang et al., 2019b): $u(\varphi = 0) = u(\varphi = 2\pi)$, $v(\varphi = 0) = v(\varphi = 2\pi)$, and $\theta(\varphi = 0) = \theta(\varphi = 2\pi)$. This yields

$$\begin{aligned} M_i \ =\ & \frac{EI}{2R\pi\left(EAR^2 + EI\right)}\Big[\,2EAR\sum v^L(2\pi) \\ & + \left(3EAR^2 + EI\right)\sum \theta^L(2\pi)\,\Big], \end{aligned} \tag{A.4}$$

$$N_i \ =\ -\frac{EI\,EA}{R\pi\left(EAR^2 + EI\right)}\left[\sum v^L(2\pi) + R\sum \theta^L(2\pi)\right], \tag{A.5}$$

$$V_i \ =\ -\frac{EI\,EA}{R\pi\left(EAR^2 + EI\right)}\sum u^L(2\pi)\,. \tag{A.6}$$

The solution for a relative rotation, $\Delta\theta_j$, at the joint located at $\varphi = \varphi_j$, reads as (Zhang et al., 2017)

$$u^L(\varphi) \ =\ -R\Delta\theta_j\sin(\varphi - \varphi_j)H(\varphi - \varphi_j)\,, \tag{A.7}$$

$$v^L(\varphi) \ =\ R\Delta\theta_j\left[1 - \cos(\varphi - \varphi_j)\right]H(\varphi - \varphi_j)\,, \tag{A.8}$$

$$\theta^L(\varphi) \ =\ \Delta\theta_j H(\varphi - \varphi_j)\,, \tag{A.9}$$

$$N^L(\varphi) \ =\ V^L(\varphi) = M^L(\varphi) = 0\,. \tag{A.10}$$

Given the present focus on rigid body displacements, the inner forces must vanish everywhere in the tunnel ring: $M(\varphi) = 0\,\text{kNm}$ and $N(\varphi) =$

$V(\varphi) = 0\,\mathrm{kN}$. Therefore, also M_i, N_i and V_i must vanish. This is an alternative way of deriving the conditions (7)–(9). Notably, Eqs. (4)–(6) can be obtained by specifying the first three rows of Eq. (A.1) for Eqs. (A.3), (A.7)–(A.9), and $M_i = N_i = V_i = 0$.

Appendix B. Derivation of the base vectors of the relative rotations resulting in rigid body displacements of the tubbings of general segmental tunnel rings

Consider a segmental ring consisting of n tubbings. Such a structure contains n joints. Scientific research by Blom (2002), El Naggar and Hinchberger (2008), as well as by Zhang et al. (2019b) suggests that the deformed configurations are governed by rigid body displacements associated with relative rotations at the joints. The latter must satisfy the continuity conditions of a ring, see Eqs. (7)–(9). Cast in matrix–vector form, these conditions read as

$$\begin{bmatrix} \sin\varphi_1 & \sin\varphi_2 & \sin\varphi_3 & \sin\varphi_4 & \dots & \sin\varphi_n \\ 1-\cos\varphi_1 & 1-\cos\varphi_2 & 1-\cos\varphi_3 & 1-\cos\varphi_4 & \dots & 1-\cos\varphi_n \\ 1 & 1 & 1 & 1 & \dots & 1 \end{bmatrix} \cdot \begin{bmatrix} \Delta\theta_1 \\ \Delta\theta_2 \\ \Delta\theta_3 \\ \Delta\theta_4 \\ \vdots \\ \Delta\theta_n \end{bmatrix} = \begin{bmatrix} 0 \\ 0 \\ 0 \end{bmatrix}, \tag{B.1}$$

The following discussion is focused on the strategy for computation of the relative rotations at the joints, $\Delta\theta_{j=1,2,\dots,n}$, representing the components of the vector $\Delta\boldsymbol{\theta}$:

$$\Delta\boldsymbol{\theta} = [\Delta\theta_1\ ;\ \Delta\theta_2\ ;\ \Delta\theta_3\ ;\ \Delta\theta_4\ ;\ \dots\ ;\ \Delta\theta_n], \tag{B.2}$$

As for $n \le 3$, the solution of $\Delta\boldsymbol{\theta}$ is unique, i.e. $\Delta\theta_{j=1,2,\dots,n} = 0$. This implies that rings consisting of three or less tubbings represent kinematically stable systems. However, in real segmental linings, n is typically larger than three.

As for $n \ge 4$, there are $n-3 > 0$ kinematic degrees of freedoms. In this case, Eq. (B.2) has infinitely many solutions. Still, solutions for $\Delta\boldsymbol{\theta}$ can be expressed in the form of a linear combination of $(n-3)$ vectors of fundamental solutions, $\Delta\boldsymbol{\theta}_{p=1,2,\dots n-3}$, which are linearly independent of each other:

$$\Delta\boldsymbol{\theta} = \alpha_1\Delta\boldsymbol{\theta}_1 + \alpha_2\Delta\boldsymbol{\theta}_2 + \dots + \alpha_{n-3}\Delta\boldsymbol{\theta}_{n-3}\,, \tag{B.3}$$

where $\alpha_{p=1,2,\dots n-3}$ represent scalar values referred to as coefficients. In the special case of symmetric segmental tunnel rings, the $n-3$ vectors of fundamental solutions may be subdivided into symmetric and antisymmetric modes of rigid body displacements, see e.g. Section 3.3.

In the general case, the $n-3$ vectors of fundamental solutions can be obtained as follows: $\Delta\boldsymbol{\theta}_{j=4,5,\dots n}$ are combined to one set of arbitrary values and inserted into Eq. (B.1). Then, $\Delta\boldsymbol{\theta}_{j=1,2,3}$ are obtained from the resulting system of equations. Casting the computed values $\Delta\boldsymbol{\theta}_{j=1,2,3}$ and the prescribed values $\Delta\boldsymbol{\theta}_{j=4,5,\dots n}$ as a vector, results in the first fundamental solution, $\Delta\boldsymbol{\theta}_1$. The remaining vectors of fundamental solutions are obtained one after another, following the same procedure, but using independent choices for $\Delta\boldsymbol{\theta}_{j=4,5,\dots n}$. Finally, $n-3$ linearly independent vectors of fundamental solutions, $\Delta\boldsymbol{\theta}_{p=1,2,3,\dots,n-3}$, are available. They form a basis. According to Tanton (2005), it can be orthonormalized as follows:

$$\boldsymbol{e}_1 = \frac{\Delta\boldsymbol{\theta}_1}{\|\Delta\boldsymbol{\theta}_1\|}, \tag{B.4}$$

$$\boldsymbol{e}_2 = \frac{\Delta\boldsymbol{\theta}_2 - (\Delta\boldsymbol{\theta}_2\cdot\boldsymbol{e}_1)\cdot\boldsymbol{e}_1}{\|\Delta\boldsymbol{\theta}_2 - (\Delta\boldsymbol{\theta}_2\cdot\boldsymbol{e}_1)\cdot\boldsymbol{e}_1\|}, \tag{B.5}$$

$$\boldsymbol{e}_3 = \frac{\Delta\boldsymbol{\theta}_3 - (\Delta\boldsymbol{\theta}_3\cdot\boldsymbol{e}_1)\cdot\boldsymbol{e}_1 - (\Delta\boldsymbol{\theta}_3\cdot\boldsymbol{e}_2)\cdot\boldsymbol{e}_2}{\|\Delta\boldsymbol{\theta}_3 - (\Delta\boldsymbol{\theta}_3\cdot\boldsymbol{e}_1)\cdot\boldsymbol{e}_1 - (\Delta\boldsymbol{\theta}_3\cdot\boldsymbol{e}_2)\cdot\boldsymbol{e}_2\|}, \tag{B.6}$$

$$\vdots$$

$$\boldsymbol{e}_{n-3} = \frac{\Delta\boldsymbol{\theta}_{n-3} - \sum_{p=1}^{n-4}(\Delta\boldsymbol{\theta}_{n-3}\cdot\boldsymbol{e}_p)\cdot\boldsymbol{e}_p}{\|\Delta\boldsymbol{\theta}_{n-3} - \sum_{p=1}^{n-4}(\Delta\boldsymbol{\theta}_{n-3}\cdot\boldsymbol{e}_p)\cdot\boldsymbol{e}_p\|}. \tag{B.7}$$

Finally, Eq. (B.3) is rewritten as

$$\Delta\boldsymbol{\theta} = \beta_1\boldsymbol{e}_1 + \beta_2\boldsymbol{e}_2 + \dots + \beta_{n-3}\boldsymbol{e}_{n-3}\,, \tag{B.8}$$

where $\beta_{p=1,2,\dots n-3}$ stand for scalar components associated with the base vectors of fundamental solutions. In matrix–vector form, the vector of relative rotation angles at the joint, $\Delta\boldsymbol{\theta}$, can be written as

$$\Delta\boldsymbol{\theta} = \mathbf{A}\cdot\boldsymbol{\beta}\,, \tag{B.9}$$

see also Eq. (10).

Appendix C. List of symbols

$\mathbf{A}$	matrix containing base vectors of relative rotations at the joints
$A_{j,i}$	an element of the base matrix $\mathbf{A}$
C	model-predicted convergence
C^{exp}	experimentally measured convergence
C_h	horizontal convergence
C_{max}	largest measured convergence in absolute terms
C_v	vertical convergence
D_o	outer diameter of the tunnel ring
$\mathbf{e}_p$	orthonormalized base vector of relative rotations at the joints ($p = 1, 2, 3, \dots, n-3$)
H	Heaviside function
h	radial thickness of the tubbings
M	bending moment
M_i	bending moment at the initial cross-section
M^L	load integral for the bending moment
N	normal force
N_i	normal force at the initial cross-section
N^L	load integral for the normal force
n	number of segmental joints
P_1	point load acting in the top and the bottom regions of the segmental tunnel ring
P_2	point load acting in the lateral regions of the segmental tunnel ring
P_3	point load acting in the intermediate regions between P_1 and P_2
R	radius of the axis of the segmental tunnel ring
u	radial component of the displacement
u_i	radial component of the displacement at the initial cross-section
u^L	load integral for the radial displacement
V	shear force
V_i	shear force at the initial cross-section
V^L	load integral for the shear force
v	circumferential component of the displacement
v_i	circumferential component of the displacement at the initial cross-section
v^L	load integral for the circumferential displacement
α_p	vector components
$\boldsymbol{\beta}$	vector, containing components associated with the base vectors of fundamental solutions for relative rotations at the joints
β_p	vector component
β_1	component associated with the symmetric mode of rigid body displacements

β_2	component associated with the first antisymmetric mode of rigid body displacements
β_3	component associated with the second antisymmetric mode of rigid body displacements
β_{1x}	x^{th} solution of β_1
β_{2x}	x^{th} solution of β_2
β_{3x}	x^{th} solution of β_3
$\Delta\theta_j$	relative rotation at the j^{th} joint
$\Delta\boldsymbol{\theta}$	vector of relative rotations at the joints
θ	cross-sectional rotation angle
θ_i	rotation angle of the initial cross-section
θ^L	load integral for the cross-sectional rotation
φ	angular coordinate of the polar coordinate system
φ_j	polar position of the j^{th} joint of the segmental tunnel ring
ψ	angular coordinate of the polar coordinate system
ψ_k	k^{th} direction in which the convergence is measured

References

Ai, Q., Yuan, Y., Bi, X., 2016. Acquiring sectional profile of metro tunnels using charge-coupled device cameras. Struct. Infrastruct. Eng. 12 (9), 1065–1075.

Blom, C., 2002. Design Philosophy of Concrete Linings for Tunnels in Soft Soils (Ph.D. thesis). Delft University of Technology, The Netherlands.

DG/TJ08-2123-2013, 2013. Code for Structural Appraisal of Shield Tunnel. Technical Report, Shanghai Municipal Commission of City Development and Transport, Shanghai (in Chinese).

El Naggar, H., Hinchberger, S., 2008. An analytical solution for jointed tunnel linings in elastic soil or rock. Can. Geotech. J. 45 (11), 1572–1593.

GB/T51438-2021, 2021. Standard for Design of Shield Tunnel Engineering. Technical Report, Ministry of Housing and Urban-Rural Development of the People's Republic of China, Beijing (in Chinese).

Huang, H., Shao, H., Zhang, D., Wang, F., 2017. Deformational responses of operated shield tunnel to extreme surcharge: a case study. Struct. Infrastruct. Eng. 13 (3), 345–360.

Jiang, Z., Liu, X., Schlappal, T., Zhang, J.-L., Mang, H.A., Pichler, B.L., 2021. Asymmetric serviceability limit states of symmetrically loaded segmental tunnel rings: hybrid analysis of real-scale tests. Tunn. Undergr. Space Technol. 113, 103832.

Jin, D., Yuan, D., Li, X., Zheng, H., 2018. An in-tunnel grouting protection method for excavating twin tunnels beneath an existing tunnel. Tunn. Undergr. Space Technol. 71, 27–35.

Li, X., Chen, X., 2012. Using grouting of shield tunneling to reduce settlements of overlying tunnels: case study in Shenzhen metro construction. J. Constr. Eng. Manage. 138 (4), 574–584.

Li, X., Lin, X., Zhu, H., Wang, X., Liu, Z., 2017. Condition assessment of shield tunnel using a new indicator: The tunnel serviceability index. Tunn. Undergr. Space Technol. 67, 98–106.

Li, P., Zhang, Y.-W., Jiang, F.-Y., Zheng, H., 2018. Comprehensive health assessment of shield tunnel structure based on prototype experiment. J. Cent. South Univ. 25 (3), 681–689.

Liu, X., Jiang, Z., Yuan, Y., Mang, H.A., 2018. Experimental investigation of the ultimate bearing capacity of deformed segmental tunnel linings strengthened by epoxy-bonded steel plates. Struct. Infrastruct. Eng. 14 (6), 685–700.

Liu, X., Jiang, Z., Zhang, L., 2017. Experimental investigation of the ultimate bearing capacity of deformed segmental tunnel linings strengthened by epoxy-bonded filament wound profiles. Struct. Infrastruct. Eng. 13 (10), 1268–1283.

Liu, X., Zhang, Y., Bao, Y., Song, W., 2022. Investigation of the structural effect induced by stagger joints in segmental tunnel linings: Numerical explanation via macro-level structural modeling. Tunn. Undergr. Space Technol. 120, 104284.

Liu, X., Zhang, J.-L., Jiang, Z., Liu, Z., Xu, P., Li, F., 2021. Experimental investigations of a segmental tunnel ring strengthened by using ultra-high performance concrete (UHPC). China J. Highw. Transp. 34 (8), 181–190 (in Chinese).

Marwan, A., Gall, V.E., Alsahly, A., Meschke, G., 2021. Structural forces in segmental linings: process-oriented tunnel advance simulations vs. conventional structural analysis. Tunn. Undergr. Space Technol. 111, 103836.

Nuttens, T., Stal, C., De Backer, H., Schotte, K., Van Bogaert, P., De Wulf, A., 2014. Methodology for the ovalization monitoring of newly built circular train tunnels based on laser scanning: Liefkenshoek Rail Link (Belgium). Autom. Constr. 43, 1–9.

Pinto, F., Whittle, A.J., 2014. Ground movements due to shallow tunnels in soft ground. I: analytical solutions. J. Geotech. Geoenviron. Eng. 140 (4), 04013040.

Tanton, J.S., 2005. Encyclopedia of Mathematics. Facts on File, New York.

T/CSPSTC 43-2019, 2019. Technical Specification for Health Monitoring of Metro Underground Structure. Technical Report, China Society for the Promotion of Science and Technology Commercialization, Beijing (in Chinese).

Xie, X., Lu, X., 2017. Development of a 3D modeling algorithm for tunnel deformation monitoring based on terrestrial laser scanning. Undergr. Space 2 (1), 16–29.

Yuan, Y., Bai, Y., Liu, J., 2012. Assessment service state of tunnel structure. Tunn. Undergr. Space Technol. 27 (1), 72–85.

Zhang, J.-L., Hellmich, C., Mang, H.A., Yuan, Y., Pichler, B., 2018a. Application of transfer relations to structural analysis of arch bridges. Comput. Assist. Methods Eng. Sci. 24 (3), 199–215.

Zhang, D.-M., Huang, Z.-K., Wang, R.-L., Yan, J.-Y., Zhang, J., 2018b. Grouting-based treatment of tunnel settlement: Practice in Shanghai. Tunn. Undergr. Space Technol. 80, 181–196.

Zhang, J.-L., Liu, X., Ren, T.-Y., Yuan, Y., Mang, H.A., 2019a. Structural behavior of reinforced concrete segments of tunnel linings strengthened by a steel-concrete composite. Composites B 178, 107444.

Zhang, J.-L., Liu, X., Zhao, J.-B., Yuan, Y., Mang, H., 2021. Application of a combined precast and in-situ-cast construction method for large-span underground vaults. Tunn. Undergr. Space Technol. 111, 103795.

Zhang, J.-L., Mang, H., Liu, X., Yuan, Y., Pichler, B., 2019b. On a nonlinear hybrid method for multiscale analysis of a bearing-capacity test of a real-scale segmental tunnel ring. Int. J. Numer. Anal. Methods Geomech. 43 (7), 1343–1372.

Zhang, J.-L., Schlappal, T., Yuan, Y., Mang, H.A., Pichler, B., 2019c. The influence of interfacial joints on the structural behavior of segmental tunnel rings subjected to ground pressure. Tunn. Undergr. Space Technol. 84, 538–556.

Zhang, J.-L., Vida, C., Yuan, Y., Hellmich, C., Mang, H., Pichler, B., 2017. A hybrid analysis method for displacement-monitored segmented circular tunnel rings. Eng. Struct. 148, 839–856.

Zhou, S., Xiao, J., Di, H., Zhu, Y., 2018. Differential settlement remediation for new shield metro tunnel in soft soils using corrective grouting method: case study. Can. Geotech. J. 55 (12), 1877–1887.

Zhu, M., Gong, X., Gao, X., Liu, S., Yan, J., 2019. Remediation of damaged shield tunnel using grouting technique: Serviceability improvements and prevention of potential risks. J. Perform. Constr. Facil. 33 (6), 04019062.